

# MR Elastography of the Liver and the Spleen Using a Piezoelectric Driver, Single-Shot Wave-Field Acquisition, and Multifrequency Dual Parameter Reconstruction

Sebastian Hirsch,<sup>1</sup> Jing Guo,<sup>1</sup> Rolf Reiter,<sup>1</sup> Sebastian Papazoglou,<sup>1</sup> Thomas Kroencke,<sup>1</sup> Juergen Braun,<sup>2</sup> and Ingolf Sack<sup>1\*</sup>

**Purpose:** Viscoelastic properties of the liver are sensitive to fibrosis. This study proposes several modifications to existing magnetic resonance elastography (MRE) techniques to improve the accuracy of abdominal MRE.

**Methods:** The proposed method comprises the following steps: (i) wave generation by a nonmagnetic, piezoelectric driver suitable for integration into the patient table, (ii) fast single-shot 3D wave-field acquisition at four drive frequencies between 30 and 60 Hz, and (iii) single-step postprocessing by a novel multifrequency dual parameter inversion of the wave equation. The method is tested in phantoms, healthy volunteers, and patients with portal hypertension and ascites.

**Results:** Spatial maps of magnitude and phase of the complex shear modulus were acquired within 6–8 min. These maps are not subject to bias from inversion-related artifacts known from classic MRE. The spatially averaged modulus for healthy liver was  $1.44 \pm 0.23$  kPa with  $\phi = 0.492 \pm 0.064$ . Both parameters were significantly higher in the spleen ( $2.29 \pm 0.97$  kPa,  $P = 0.015$  and  $0.749 \pm 0.144$ ,  $P = 6.58 \cdot 10^{-5}$ , respectively).

**Conclusion:** The proposed method provides abdominal images of viscoelasticity in a short time with spatial resolution comparable to conventional MR images and improved quality without being compromised by ascites. The new setup allows for the integration of abdominal MRE into the clinical workflow.

**Magn Reson Med** 71:267–277, 2014. © 2013 Wiley Periodicals, Inc.

**Key words:** 3D multifrequency MRE; least-squares inversion; piezoelectric driver; shear waves; complex shear modulus; loss tangent; liver; portal hypertension

## INTRODUCTION

Hepatic fibrosis is associated with significantly elevated liver stiffness. Therefore, elastography based on ultrasound (1,2) or magnetic resonance imaging (3,4) has been established during the last decade as a noninvasive marker of liver fibrosis.

In elastography, the tissue is mechanically excited by static compression, focused acoustic radiation, or gentle vibrations in the low frequency range below 100 Hz (5–7). The latter type of stimulation is exploited in magnetic resonance elastography (MRE), which relies on the evaluation of shear wave fields in two or three dimensions (8–10). With its capability of capturing any component of the wave field within arbitrarily angulated imaging planes or in 3D slabs, MRE is currently the most precise elastography technique for staging hepatic fibrosis (11). Furthermore, the mechanical properties of the spleen attainable by an MRE scan of the liver have been proven sensitive to hepatic portal hypertension and can thus provide additional diagnostic information (12).

However, only a few sites worldwide have established MRE of the liver as a routine clinical procedure. One major limitation of clinical MRE is the current driver technology, which relies on Lorentz coils (13) or loudspeakers (14,15), imposing either field distortions, which limit the applicability of fast echo-planar-imaging (EPI) sequences, or requiring rods and tubes for the transmission of vibrations from distant wave sources to the liver (10,14). Interference-free, nonmagnetic drivers have been proposed in the past, however, without being optimized and tested for applications in abdominal MRE (16,17).

A further obstacle is that spatial maps of viscoelastic parameters still lack consistency. These so-called elastograms (18–24) are regularly limited by severe artifacts due to wave nodes or low amplitudes, resulting in unreliable regions within the liver because no elastic deformation can be achieved. Such uncertain regions have to be identified and masked to avoid biased stiffness estimates.

To overcome these limitations, we here introduce a setup and protocol which incorporates a semidistant driver placed at the end of the patient table, fast 3D EPI-based acquisition of vibration fields at multiple drive frequencies, and a single-step inversion algorithm of multifrequency 3D wave-field data. While the driver and the imaging sequence are novel in the application to the liver and to the spleen, we will introduce an inversion algorithm that is of general interest in multifrequency MRE. Our aim is an improved spatial resolution of abdominal MRE given by reduced inversion errors and less regions suffering from uncertain viscoelasticity values. This, combined with short examination times and improved driver handling, aids the further advancement of abdominal MRE towards a precise clinical modality for staging hepatic fibrosis or mechanically characterizing lesions and tissue heterogeneities in the abdomen.

<sup>1</sup>Department of Radiology, Charité—Universitätsmedizin Berlin, Campus Charité Mitte, Berlin, Germany.

<sup>2</sup>Institute of Medical Informatics, Charité—Universitätsmedizin Berlin, Campus Benjamin Franklin, Berlin, Germany.

\*Correspondence to: Ingolf Sack, Ph.D., Department of Radiology, Charité—Universitätsmedizin Berlin, Charitéplatz 1, 10117 Berlin, Germany. E-mail: ingolf.sack@charite.de

Received 26 October 2012; revised 10 January 2013; accepted 10 January 2013

DOI 10.1002/mrm.24674

Published online 14 February 2013 in Wiley Online Library (wileyonlinelibrary.com).

© 2013 Wiley Periodicals, Inc.

In the following chapter, we will introduce the new inversion method for the reconstruction of two mechanical parameters, one of which is related to the viscosity of the material while the other one dominantly reflects the elastic behavior of the tissue. The parallel reconstruction of both parameters by two separated single-step multifrequency inversion algorithms motivated the term multifrequency dual elastovisco (MDEV) inversion.

In the “Methods” section, further details on hardware, imaging sequence and data processing will be explained. Results are presented for 10 healthy male volunteers and four patients with portal hypertension. We chose this group of patients because portal hypertension is frequently associated with ascites, which challenges the transmission of shear waves to the liver. Finally, the key points of the method are discussed and summarized.

### Multifrequency Dual Elastovisco Inversion

The basic idea of multifrequency wave inversion was proposed in (25) and is based on least-squares analysis of 2D wave data within a certain dynamic range. The reconstructed shear modulus map is related to the springpot model and therewith influenced by the viscous properties of the tissue (26). In MDEV inversion, we pursue a different route and investigate the phase and the magnitude of the complex shear modulus  $G^*$  by two independent steps of wave inversion.

To introduce MDEV inversion, we denote the real and imaginary parts of any complex quantity by prime and double prime as it is common for the notation of the complex shear modulus:

$$G^* = G' + iG'' \quad [1]$$

$G'$ , the storage modulus, is the classical parameter measured in MRE. It describes the elastic properties of a material, while the loss modulus,  $G''$ , refers to its viscous properties. The MDEV inversion is based on the representation of  $G^*$  by its magnitude  $|G^*|$  and phase  $\phi$ :

$$G^* = |G^*|(\cos \phi + i \sin \phi) \quad [2]$$

Similar to  $G'$ ,  $|G^*|$  is related to our haptic sensation of the stiffness or softness of a material, while the phase

angle of the complex modulus  $\phi = \arctan(G''/G')$  is sensitive to the geometry of the viscoelastic lattice (27). According to the theory of viscoelastic scaling,  $\phi$  relates to the viscoelastic powerlaw constant (28) (also referred to as “loss tangent”) which can be directly linked to structure-relevant terms like “fractal network dimension” or “network density” unlike classical viscoelastic parameters which are based on homogeneous material models (27).

In this study, we strive for high spatial resolution and reduced inversion artifacts in abdominal maps of  $|G^*|$  and  $\phi$ . Our strategy is to merge information of multifrequency wave fields of several MRE scans into generalized frequency-independent maps of  $|G^*|$  and  $\phi$ . Thereby, the frequency dispersion of the shear modulus of liver (15,26,29–31) within our range of vibration frequencies (30–60 Hz) is averaged out.

Furthermore, we apply the assumption of local homogeneity (18) which allows us to separate  $G^*$  from spatial derivatives in the Helmholtz-equation:

$$G^* \Delta u_m^*(\mathbf{r}, \omega_n) = -\rho \omega_n^2 u_m^*(\mathbf{r}, \omega_n) \quad [3]$$

$\rho$  is the material density,  $u_m^*$  is the  $m$ -th component of the complex shear wave field at position  $\mathbf{r}$ . The index  $n$  denotes the  $n$ -th harmonic angular excitation frequency  $\omega_n$  and  $\Delta$  is the 3D-Laplacian operator. Equation [3] can be rewritten in terms of  $|G^*|$  and  $\phi$  following the notation of (25):

$$|G^*| \begin{bmatrix} \cos \phi & -\sin \phi \\ \sin \phi & \cos \phi \end{bmatrix} \Delta \mathbf{x}_{mn} = -\rho \omega_n^2 \mathbf{x}_{mn} \text{ with } \mathbf{x}_{mn} = \begin{bmatrix} u_m'(\omega_n) \\ u_m''(\omega_n) \end{bmatrix} \quad [4]$$

### Multifrequency Recovery of $\phi$

As can be seen from Eq. [4], the Laplace operator causes a scaled rotation of the vector  $\mathbf{x}_{mn}$  with angle  $\phi$ . Thus, the scalar-product of  $\Delta \mathbf{x}_{mn}$  and  $\mathbf{x}_{mn}$ ,

$$\Delta \mathbf{x}_{mn} \cdot \mathbf{x}_{mn} = -|\Delta \mathbf{x}_{mn}| |\mathbf{x}_{mn}| \cos \phi, \quad [5]$$

can be solved for  $\phi$  in a least-squares sense:

$$\phi = \arccos \left( -\frac{\sum_{m=1}^3 \sum_{n=1}^N [\Delta u_m'(\omega_n) u_m'(\omega_n) + \Delta u_m''(\omega_n) u_m''(\omega_n)] |\Delta u_m^*(\omega_n)| |u_m^*(\omega_n)|}{\sum_{m=1}^3 \sum_{n=1}^N (|\Delta u_m^*(\omega_n)| |u_m^*(\omega_n)|)^2} \right) \quad [6]$$

### Multifrequency Recovery of $|G^*|$

Having analyzed the rotation of  $\mathbf{x}$  due to the Laplace operator, we now address its change in length. It is sufficient to solve the magnitude of the Helmholtz equation (Eq. [3]),

$$|G^*| |\Delta u_m^*(\mathbf{r}, \omega_n)| = \rho \omega_n^2 |u_m^*(\mathbf{r}, \omega_n)|, \quad [7]$$

in a similar manner as given by Eq. [6]:

$$|G^*| = \rho \frac{\sum_{m=1}^3 \sum_{n=1}^N \omega_n^2 |\Delta u_m^*(\omega_n)| |u_m^*(\omega_n)|}{\sum_{m=1}^3 \sum_{n=1}^N |\Delta u_m^*(\omega_n)|^2} \quad [8]$$

## METHODS

### Materials and Subjects

To demonstrate MDEV inversion, a gelatin phantom was prepared and studied by MRE. In the phantom, three

spherical gelatin inclusions (gelatin/water ratio 80 g/L, 150 g/L, and 220 g/L) of 2 cm diameter were embedded in a gelatin matrix (gelatin/water ratio 190 g/L). In the following, the three inclusions are numbered as inclusion 1, 2, and 3 with increasing gelatin/water ratio.

In vivo liver MRE was applied to 10 healthy volunteers (three females, age range from 22 to 51 years) and four patients with portal hypertension (two females, age range from 58 to 75 years, portosystemic pressure gradients of 32, 18, 12, 27 mmHg from patients #1 to #4, respectively) after approval was obtained from the internal review board. Volunteer #1 was examined five times in one day, each measurement separated by approximately 1 h to test the reproducibility of our method.

### Wave Generator

A custom-designed nonmagnetic driver based on piezoelectric ceramics as proposed by (16) was adapted to be fixed to the end of the patient table (Fig. 1). Vibration amplitudes of a vertical piezoelectric ceramic stack of 0.18 mm (180 mm length, 150 V, 63  $\mu$ F, 3.5 kN; Piezosystem, Jena, Germany) were amplified by a horizontal 40 cm lever arm to maximum deflection amplitudes of approximately 2–3 mm. The vibrations were transferred from the tip of the lever to the patient by a carbon fiber rod connected at its distal end to a rubber mat. The transducer mat was moderately pressed onto the body surface in the position just below the right costal arch using Velcro strips attached to the patient table.

### Imaging Sequence

All experiments were conducted on a 1.5 T magnetic resonance imaging scanner (Magnetom Sonata; Siemens Erlangen, Germany) equipped with a 12-channel phased

array surface coil. A 2D single-shot spin-echo EPI sequence with a trapezoidal flow-compensated motion-encoding gradient (MEG) consecutively applied along all three axes of the scanner coordinate system was used for rapid motion field acquisition. The motion was initiated by a trigger pulse from the scanner at least 100 ms before the start of the MEG to allow the wave to propagate into the tissue. Eight dynamics of a wave cycle were captured by delaying the trigger pulse in increments of  $1/(8f)$  with  $f$  being the vibration frequency. Vibration frequencies were 30, 40, 50, and 60 Hz. In contrast to multifrequency MRE as proposed in (30,31) we used single-frequency stimuli which potentially provide higher mechanical displacement amplitudes inside the liver than superimposed multifrequency waveforms. For each drive frequency, MEG-direction and wave dynamic, 10 adjacent transversal image slices of  $2.7 \times 2.7 \times 5 \text{ mm}^3$  resolution were recorded yielding a total of 960 images. Data acquisition was split into 12 breath holds of 15 sec each. Within one such period, 10 slices, eight time steps and one wave component at one vibration frequency could be acquired. Total examination time was 6–8 min. Further imaging parameters: repetition time, 182 ms; echo time, 54 ms; field of view (FoV),  $350 \times 284 \text{ mm}^2$ ; matrix size  $128 \times 104$ ; parallel imaging with GRAPPA factor 2; MEG frequency, 50 Hz (implying fractional motion encoding for all drive frequencies  $\neq 50 \text{ Hz}$  (32) and providing a feasible compromise between motion sensitivity and short echo time); MEG amplitude, 30 mT/m. A schematic of the imaging sequence is shown in Figure 2.

For the phantom experiments, the vibration frequency and the spatial resolution had to be adjusted to account for the significantly higher stiffness of the phantom. The resolution was  $1.5 \times 1.5 \times 1.5 \text{ mm}^3$  and the vibration frequencies were 110, 120, 130, and 140 Hz.



FIG. 1. Nonmagnetic driver for MRE of liver. A close view of the driver, which is placed at the end of the patient table, is shown in the left image. A carbon fiber rod is mounted to the horizontal lever arm for efficient wave transmission to the transducer mat (shown in the upper right image). The entire setup is shown in the bottom right figure. The vibration direction is indicated by arrows.

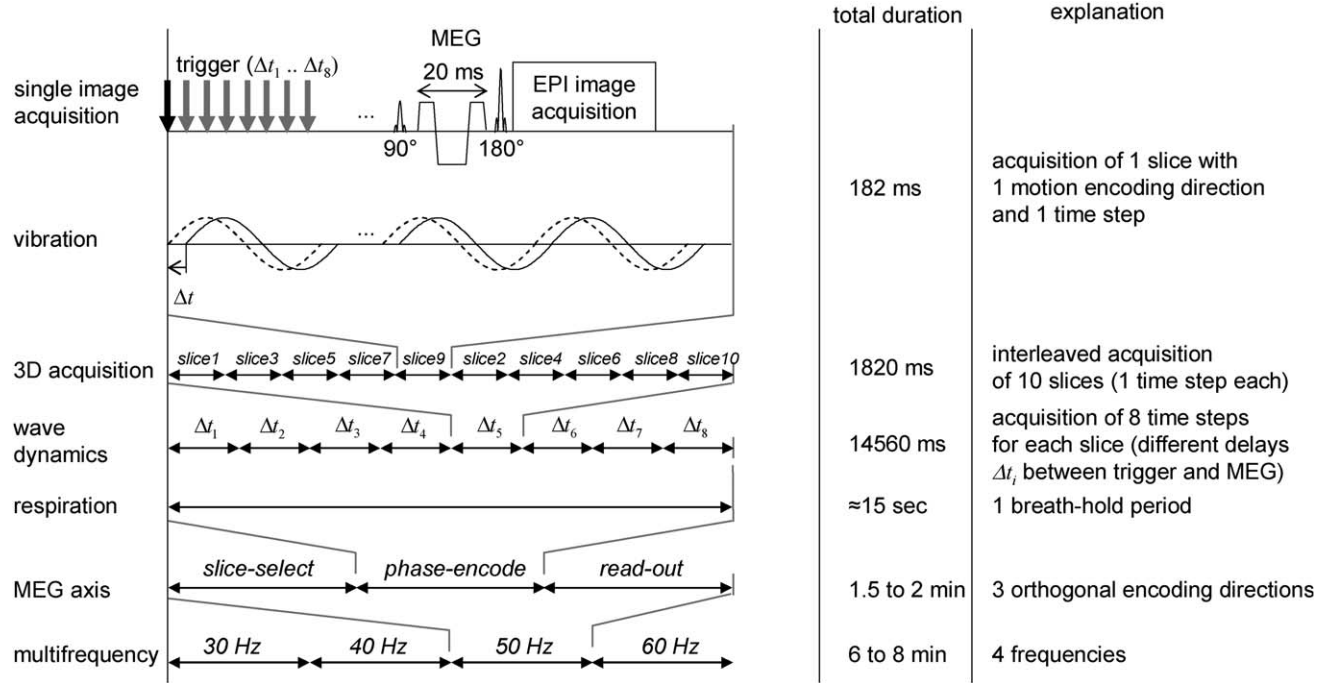


FIG. 2. Sequence timing diagram for acquisition of wave fields (three Cartesian motion components) in 10 slices at eight time points ( $\Delta t_{1..8}$ ) during a vibration period  $1/f$ . The durations indicated in the third column include free breathing periods between measurements.

### Data Post Processing

Figure 3 illustrates data post processing from raw phase data to complex wave images used for the inversions given in Eqs. [6] and [8]. In a first step, gradient-based unwrapping was performed as proposed by (33), i.e., first-order spatial derivatives of the spin phase  $\phi_m$  were calculated by

$$\frac{\partial \phi_m(\mathbf{r}, \omega_n)}{\partial x_k} = -i \cdot \exp[-i\phi_m(\mathbf{r}, \omega_n)] \cdot \frac{\partial}{\partial x_k} \exp[i\phi_m(\mathbf{r}, \omega_n)]. \quad [9]$$

$\phi_m$  is wrapped ( $\phi_m \in [0, 2\pi)$ ) while its derivative is wrap-free and unbiased if the phase difference of two adjacent voxels does not exceed  $\pi$ .  $\partial \phi_m / \partial x_k$  was scaled to  $\partial u_m / \partial x_k$  by the factor given in Eq. [4b] of (34).

For reducing noise, numerical derivatives were calculated by 3D gradients according to Anderssen and Hegland (35) using a two-pixel symmetric window in three dimensions (36). The resulting strain components of the wave field were used to calculate the curl field, as has been established in 3D MRE for suppressing volumetric strain (37). The curl components  $C_1$ ,  $C_2$ , and  $C_3$  are defined as follows:

$$C_1 = \frac{\partial u_3}{\partial x_2} - \frac{\partial u_2}{\partial x_3}; C_2 = \frac{\partial u_1}{\partial x_3} - \frac{\partial u_3}{\partial x_1}; C_3 = \frac{\partial u_2}{\partial x_1} - \frac{\partial u_1}{\partial x_2}. \quad [10]$$

where the indices 1, 2, and 3 refer to the imaging gradient directions of read-out, phase-encoding, and slice selection. The curl components of Eq. [10] were taken as filtered shear wave fields (no further filter was applied) and Fourier-transformed along the time axis (eight samples over a vibration cycle). The wave image corresponding to

the first harmonic, i.e.,  $u_m^*(\mathbf{r}, \omega_n)$  was selected for parameter recovery according to Eqs. [6] and [8]. The density of the liver was assumed to be  $1.1 \text{ g/cm}^3$  (38) and the Laplacian was calculated using a standard one-dimensional gradient scheme within a single-pixel neighborhood. The regions of interest outlining the liver margins or the inclusion boundaries in the phantom were manually placed based on the magnitude images of the MRE scan. Statistical significance was assessed by a two-sided Student's  $t$ -test with a level of significance of 0.05.

### RESULTS

Figure 4 illustrates the improvement of MRE parameter maps by adding more information to the wave-field inversion, demonstrated for the gelatin phantom. The far left and the far right column show the results of algebraic Helmholtz inversion for a single frequency (130 Hz). Instead of single wave components  $u_m^*(\mathbf{r}, \omega_3)$ , we incorporated the curl components  $C_m^*(\mathbf{r}, \omega_3)$  from Eq. [10], which requires the application of 3D vector-field MRE. Therefore, these images do not fully compare to 2D scalar MRE, although it has been shown that appropriate high-pass filtering can produce similar results (39). It is clearly visible that single-component, single-frequency information does not provide sufficient spatial resolution to differentiate the three inclusions from the matrix. The resolution is improved by combining three curl-components into single-frequency parameter maps, which were calculated by Eqs. [6] and [8] without the summation over index  $n$ . However, particularly in  $\phi$ , single-frequency maps still appear affected by artifacts not seen after full multifrequency inversion. We estimated the standard deviation (SD) for both  $|G^*|$  and  $\phi$  over the



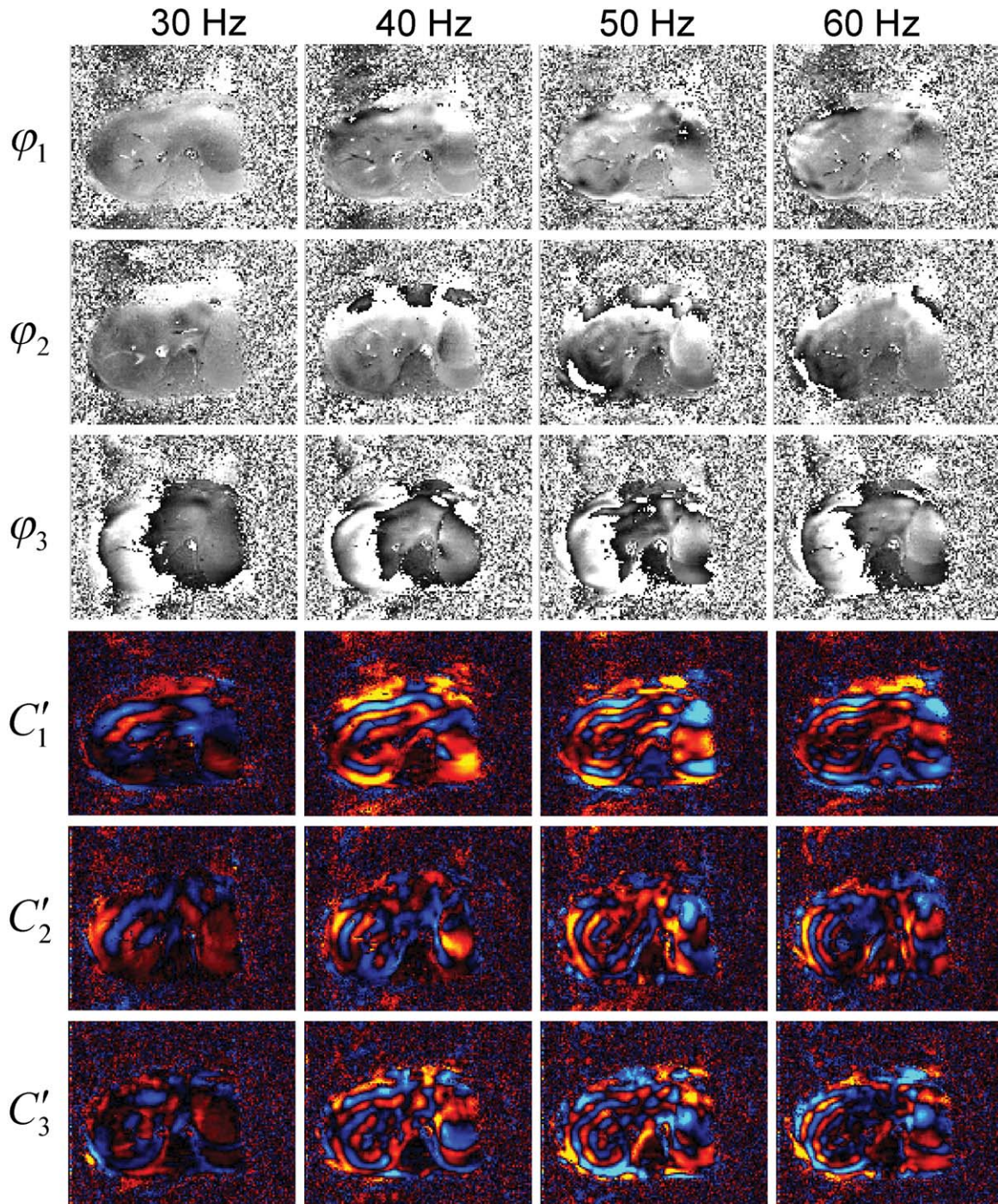


FIG. 3. Post-processing in multifrequency 3D MRE. Gray-scale images  $\phi_m$ : Wrapped raw phase data (three components) in one transversal slice and for one time point. Color-encoded images  $C'_m$ : Curl components (after Fourier transformation) calculated according to Eqs. [9] and [10] using 3D-gradients proposed in Ref. 35. Note that no further filter is applied—the wave images are directly used for MDEV inversions given in Eqs. [6] and [8].

phantom matrix as a measure of parameter map inhomogeneity being mainly caused by artifacts and therefore indicating the quality of the inversion. SD-values of  $|G^*|$  and  $\phi$  in Figure 4 column (c) incorporating all frequencies and components are 40% and 50% of the mean  $|G^*|$  and  $\phi$  values, respectively. All components at single-frequency parameter maps [Fig. 4 column (b) and (d)] yield SD-values of 50% (for  $|G^*|$ ) and 80% ( $\phi$ ) with respect to

the averaged values. For the single-curl, single-frequency inversion the SD of both  $|G^*|$  and  $\phi$  are in the order of the mean values [Fig. 4 column (a) and (e)]. The full MDEV-inversion not only enables us to distinguish all inclusions from the matrix, their relative order of intensities in the  $|G^*|$  map but also reveals their relative compositions: Inclusion 3 is firmest with the highest gelatin/water ratio and consequently it appears brightest

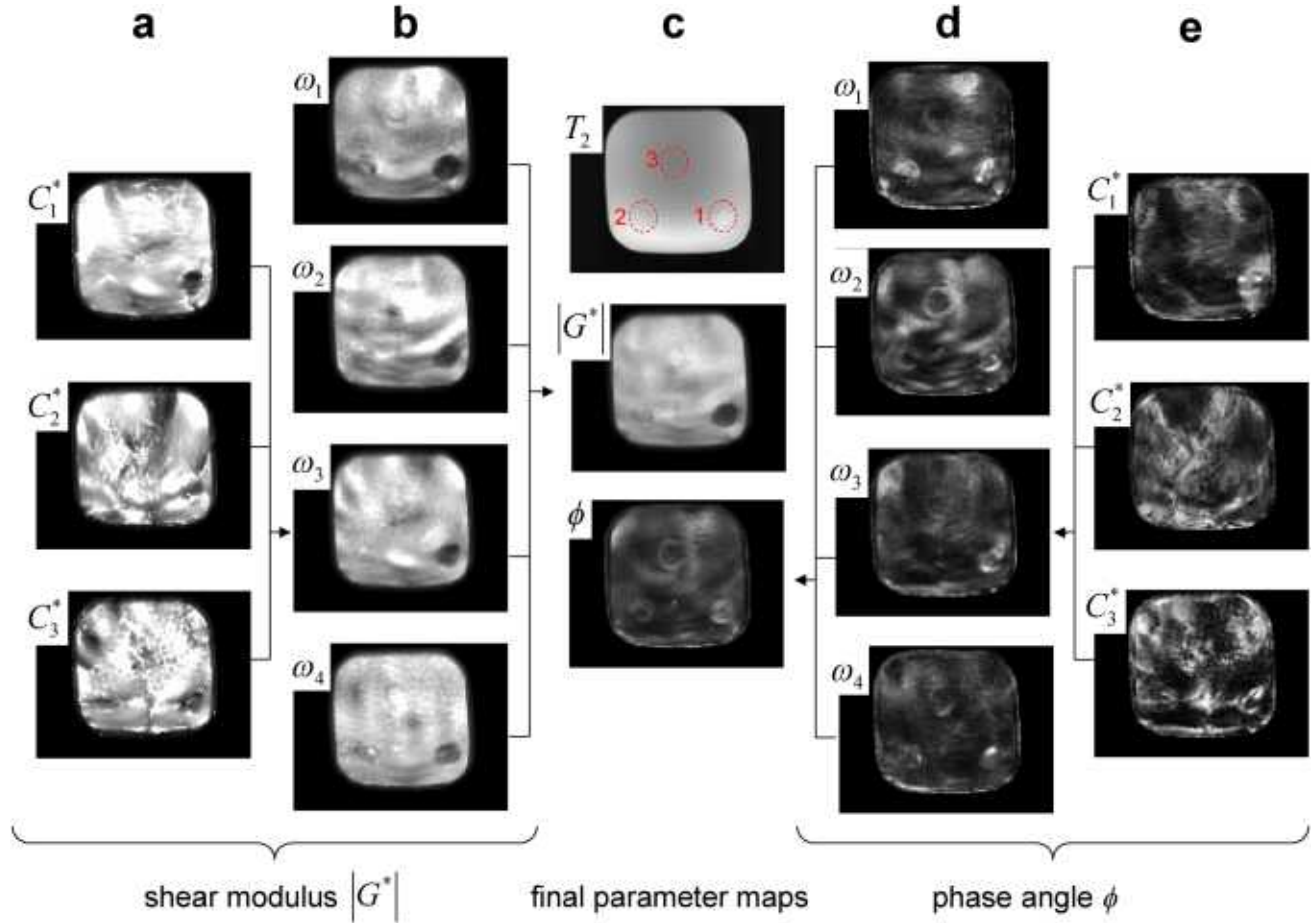


FIG. 4. Improvement of the image quality in MRE parameter maps of a gelatin phantom by adding elastodynamic information to the calculation of  $|G^*|$  and  $\phi$  (all images were averaged over six adjacent slices). Columns (a) and (b) show the reconstruction of  $|G^*|$ , based on single curl-components  $C_m^*$  at drive frequency 130 Hz (a) and combining three curl-components  $C_{1,3}^*$  at each single drive frequency ( $\omega_{1,4} = 110$  Hz, 120 Hz, 130 Hz, and 140 Hz) (b). The final  $|G^*|$ -map is the second image in column (c) in which all the information of  $C_{1,3}^*$  and  $\omega_{1,4}$  is incorporated. Correspondingly, the reconstruction of  $\phi$  is illustrated in columns (d) and (e) with the final map shown in the third image of (c). For anatomical comparison, the  $T_2$ -weighted magnitude image of an MRE scan is shown in column (c). The three inclusions are encircled and numbered with increasing gelatin/water ratio. Note that this is a schematic diagram indicating the flow of information, not the actual reconstruction pipeline. In practice, the module maps in column (c) are calculated directly according to Eqs. [6] and [8], without intermediate parameter maps for individual frequencies being obtained. [Color figure can be viewed in the online issue, which is available at [wileyonlinelibrary.com](http://wileyonlinelibrary.com).]

( $|G^*| = 42.8 \pm 6.7$  kPa). Inclusion 2 is similar to the matrix (inclusion 2:  $|G^*| = 26.6 \pm 3.5$  kPa; matrix:  $|G^*| = 27.9 \pm 11.4$  kPa) while inclusion 1 appears dark ( $|G^*| = 11.5 \pm 2.4$  kPa) due to the lowest gelatin/water ratio.

In Figure 5, we address the effect of averaging to MDEV inversion. The left column repeats the  $|G^*|$ - and  $\phi$ -map of Figure 4 labeled by  $\omega_1$ , i.e., single-frequency inversion with  $N=1$  in Eq. [8]. In addition, the maps were averaged over six slices for noise reduction. The right column of Figure 5 shows images calculated by MDEV inversion, i.e.,  $N=4$  in Eq. [8], however, in contrast to Figure 4, the  $|G^*|$ - and  $\phi$ -map are not averaged. Thus, the left column of Figure 5 represents MDEV inversion with less information involved than used for single-frequency (DEV) inversion (four frequencies versus six averages). As can be seen, the multifrequency parameter maps contain less wave residues and provide a better representation of the relative order of inclusion stiffnesses than DEV-inversion.

Figure 6 has the same structure as Figure 4; it illustrates the improvement of MRE parameter maps of the liver in a single subject. The image quality of single-frequency, single-component maps is insufficient for the discrimination of anatomical details within the liver. MDEV inversion based on the full experimental information on the other hand yields maps of  $|G^*|$  and  $\phi$  with anatomical details such as vena cava and aorta.

Figure 7 shows sets of MRE parameter map of one healthy volunteer and one patient. Liver and parts of the spleen are well resolved by  $|G^*|$  and  $\phi$ . It is remarkable that areas of larger vessels as inferior vena cava or abdominal aorta are visually characterized by low intensity in the  $|G^*|$ -maps, revealing the low shear modulus of such fluid-filled compartments. In agreement with the literature (40), a higher degree of heterogeneity is observable for diseased liver in both  $|G^*|$ - and  $\phi$ -maps when compared to the healthy liver. In Figure 8, a central slice of MRE data of the patient from Figure 7 is shown along with T1- and



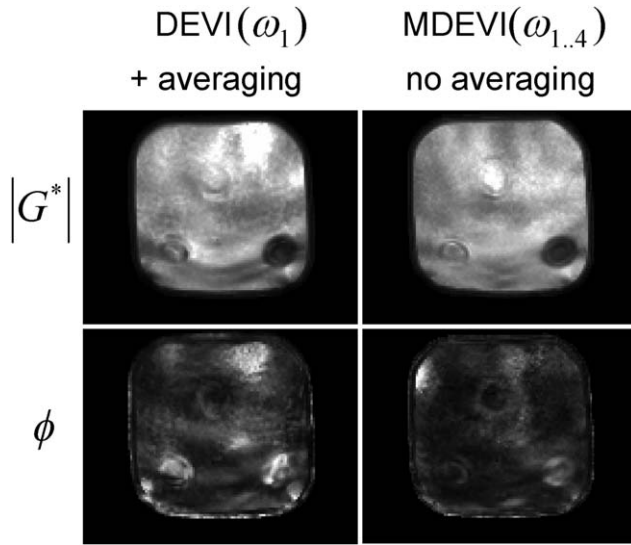


FIG. 5. MRE parameter maps obtained from single-frequency and multi-frequency dual elastovisco inversion, DEVI and MDEVI, respectively. The DEVI-maps correspond to the images shown in Figure 4 at  $\omega_1$  (110 Hz vibration frequency) which include six averaged slices. In contrast, MDEVI includes all vibration frequencies  $\omega_{1..4}$  (110–140 Hz) but in a single slice. Although no averaging was applied, the quality of MDEVI-images is still comparable with the final parameter maps of Figure 4 and clearly better than the result of single-frequency inversion shown in the left column even though less information was involved (note the wave residues and the relative stiffnesses of the inclusions).

T2-weighted magnetic resonance imaging for better illustrating the resolution of viscoelastic details in this image slice.

We can use the intrahepatic SDs given in Table 1 for quantifying heterogeneity. In agreement with the apparent heterogeneity of  $|G^*|$  and  $\phi$  visible in Figure 7, their SD-values are generally lower in healthy volunteers than in patients (SD of  $|G^*| = 0.54 \pm 0.09$  kPa [volunteers], SD of  $|G^*| = 1.07 \pm 0.61$  kPa [patients],  $P = 0.015$ ; SD of  $\phi = 0.247 \pm 0.041$  [volunteers], SD of  $\phi = 0.341 \pm 0.019$  [patients],  $P = 0.001$ ).

Notably, with  $\phi = 0.803 \pm 0.094$ , patients have significantly higher  $\phi$ -values compared to healthy volunteers ( $\phi = 0.492 \pm 0.064$ ,  $P = 1.1 \cdot 10^{-5}$ ), whereas the group-mean shear modulus  $|G^*|$  is not altered between our groups (volunteers:  $1.44 \pm 0.23$  kPa, patients:  $1.96 \pm 0.99$  kPa,  $P = 0.129$ ). The high shear modulus in patient #1 ( $|G^*| = 3.36 \pm 1.82$  kPa) is likely due to fibrosis as discussed later.

As in the liver, splenic  $|G^*|$  is not distinguishable between the groups (volunteers:  $2.29 \pm 0.97$  kPa, patients:  $2.58 \pm 0.67$  kPa,  $P = 0.594$ ) whereas  $\phi$  differs (volunteers:  $0.749 \pm 0.144$ , patients:  $1.012 \pm 0.100$ ,  $P = 0.0066$ ).

In the group of healthy volunteers, both parameters  $|G^*|$  and  $\phi$  are higher in the spleen than in the liver ( $P = 0.015$  and  $6.58 \cdot 10^{-5}$ , respectively). In the same group, a significant correlation between splenic and hepatic stiffness ( $|G^*|$ ) exists, as illustrated by Pearson's linear correlation coefficient ( $R = 0.8488$ ,  $P = 0.002$ ) which agrees with literature values (41). However, no such correlation between splenic and hepatic MRE constants was found for  $\phi$  or for both  $|G^*|$  and  $\phi$  in patients.

In alignment with the literature (12), portosystemic pressure seems to be correlated with MRE parameters, such as  $|G^*|$  ( $R = 0.774$ ) or  $\phi$  ( $R = 0.882$ ), however, due to the low number of patients no statistical significance was attained.

All MRE constants of liver and spleen are summarized in Table 1. The table also addresses the reproducibility of the experiments by showing results of five repeated measurements in volunteer #1. Since the five scans were separated by hours with replacing the volunteer and the actuator each time, the low SD within these scans ( $|G^*| = 1.58 \pm 0.11$  kPa,  $\phi = 0.419 \pm 0.046$ ) validates the high reproducibility of the method.

## DISCUSSION

This study is aimed at contributing to the advancement of liver MRE by introducing an improved driver technology, imaging sequence, and reconstruction method. The semidistant driver used here provided similar characteristics as the loudspeaker-based setup published in (10), with sufficiently high shear wave amplitudes (in the range of 10–100  $\mu\text{m}$ ) in all subjects without limitations imposed by abdominal fat or ascites. The transducer position could easily be adjusted outside the scanner bore and no apparent field distortions interfered with our EPI-based wave-field acquisition. On-site driver technologies, such as Lorentz coils, have been combined with multishot gradient-echo sequences (42) but have not been used for fast single-shot EPI-MRE before. Fast single-shot EPI-MRE permits, for the first time, 3D vector-field MRE at four frequencies in a short time of 12 breath holds. The acquired elastodynamic information combines former approaches of 3D MRE (13,40) with 2D multifrequency MRE (15,31). The strength of 3D MRE is its robustness against changes of wave polarization at tissue interfaces, whereas 2D multifrequency MRE can measure the dispersion of  $G^*$  over frequency and alleviates signal blanks and amplitude nulls present in single-frequency wave patterns. Our inversion routine defined by Eqs. [6] and [8] incorporates independently acquired information yielding an overdetermined system of equations, which are solved in a least-squares sense (25). By adding experimental information to the calculation of parameter maps, their quality is improved as seen in Figures 4 and 8. In Figure 4 column (c), three inclusions can be easily distinguished from each other as well as from the matrix in the parameter maps. In Figure 8, by comparison with the T1- and T2-weighted images, anatomic features such as inferior vena cava, descending aorta, falciform ligament, and ascites are resolved in the  $|G^*|$  and  $\phi$ -maps.

The mean value of  $|G^*| = 1.44 \pm 0.23$  kPa found for healthy volunteers agrees with  $|G^*|$  estimated from values obtained by 2D multifrequency MRE (31). In the latter, a real-part modulus  $G' = 1.97 \pm 0.55$  kPa averaged over a frequency range between 25 and 62.5 Hz was reported. Combined with the corresponding  $G'' = 0.75 \pm 0.18$  kPa we obtain  $|G^*| = 2.11 \pm 0.58$  kPa, which is within our SD margins. In general, multifrequency MRE parameters cannot directly be compared with MRE values measured at a single vibration frequency (9,13,14,40,42–44). It is therefore necessary to translate thresholds used in single-

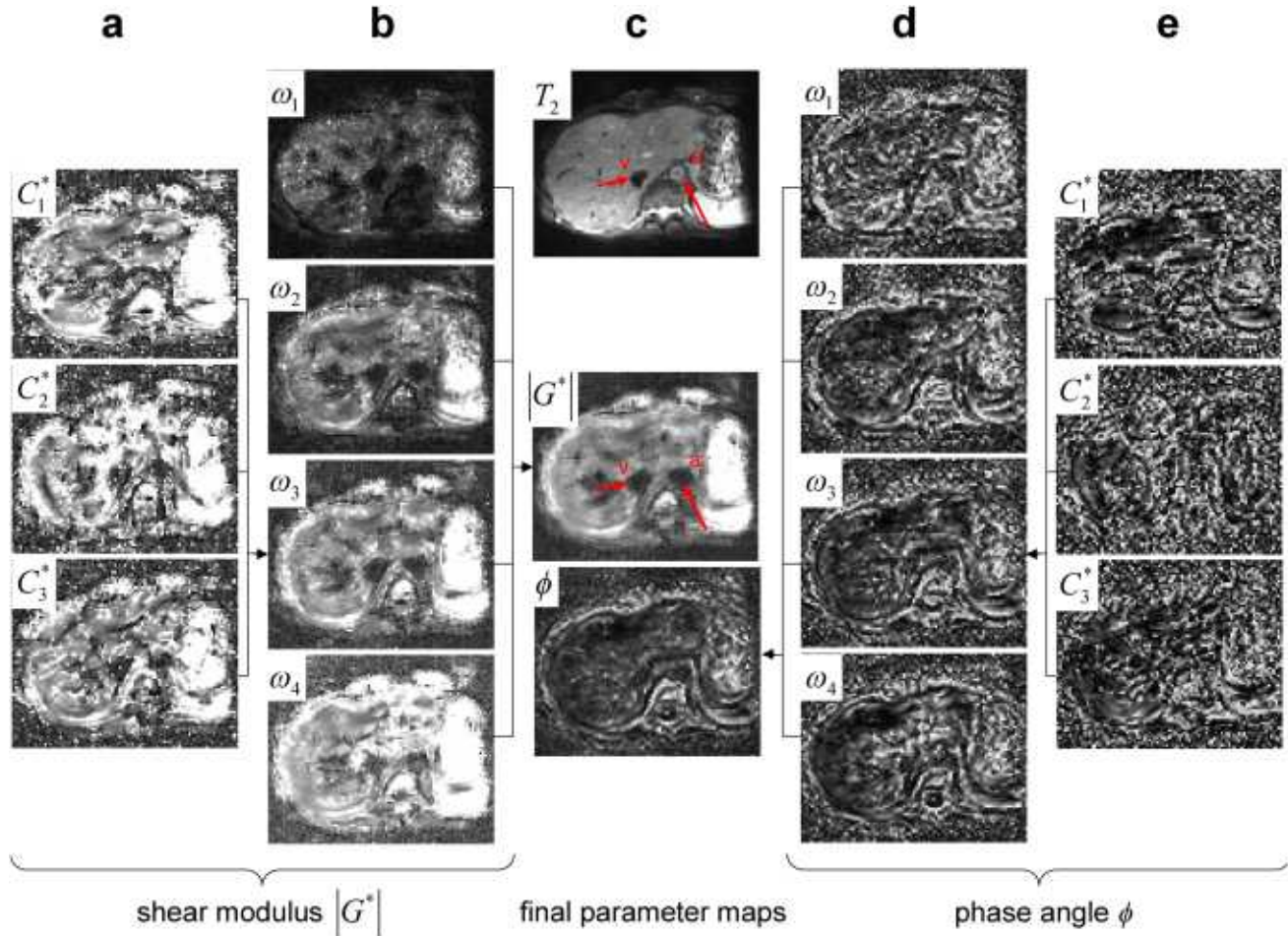


FIG. 6. Flow of information for the MRE parameter reconstruction in the liver of a healthy volunteer, in analogy to Figure 4. The curl components in column (a) were acquired at 50 Hz; the dynamic range was  $\omega_{1..4} = (30 \text{ Hz}, 40 \text{ Hz}, 50 \text{ Hz}, \text{ and } 60 \text{ Hz})$ . For anatomical comparison, a  $T_2$ -weighted magnitude image of an MRE scan is shown in column (c). The vena cava and the aorta descendents are labeled with “v” and “a”, respectively. [Color figure can be viewed in the online issue, which is available at [wileyonlinelibrary.com](http://wileyonlinelibrary.com).]

frequency MRE for staging hepatic fibrosis to our multifrequency protocol. In this process, it remains to be determined whether the thresholds proposed in Ref. 31 can be adopted by our new 3D multifrequency protocol.

It is a stimulating result of this study that we could resolve hepatic and splenic stiffness from the same scan in all subjects including those with ascites. The higher  $\phi$  in the spleen suggests that the spleen has a more strongly cross-linked mechanical structure than the liver. Given that nearly 80% of the spleen is made up of red pulp, which consists of fibrils and connective tissue cells, it is not surprising that splenic  $\phi$  is significantly higher. Our study reproduces the correlation of splenic and hepatic stiffness reported in (12,41). However, the lack of correlation between splenic and hepatic  $\phi$  suggests that  $|G^*|$  in both organs is sensitive to mechanisms which do not alter the inherent tissue architecture such as changing vascular pressure, interstitial fluid accumulation, or strengthening of connective tissue. However, further conclusions require the investigation of more subjects and an in-depth analysis of  $|G^*|$  and  $\phi$  under different physiological and pathological conditions, which is beyond the scope of this feasibility study.

A limitation of our study is the small number of patients and the lack of information about possible hepatic fibrosis in our patient group. One of our patients had a significantly higher hepatic stiffness than the other subjects, indicating severe fibrosis. However, since biopsy was clinically not indicated in our cohort, we can provide no explanation for this high  $|G^*|$  value. Our study was intended to provide the technical background for high-resolution 3D MRE of the liver, which ultimately needs to be applied and validated in a large cohort of patients with well-classified hepatic fibrosis.

In summary, 3D multifrequency MRE including non-magnetic shear wave excitation and least-squares multifrequency inversion was introduced for improving spatial resolution of liver MRE. The proposed method is suitable for the reproducible measurement of spatially resolved viscoelastic parameter maps in liver and spleen with minimized inversion-related artifacts. Using the new protocol the combined elastodynamic information of 3D MRE and multifrequency MRE can be acquired in a total acquisition time of 12 breath holds. The piezoelectric driver can be integrated into the scanner. Therefore, the entire setup may support the clinical use of



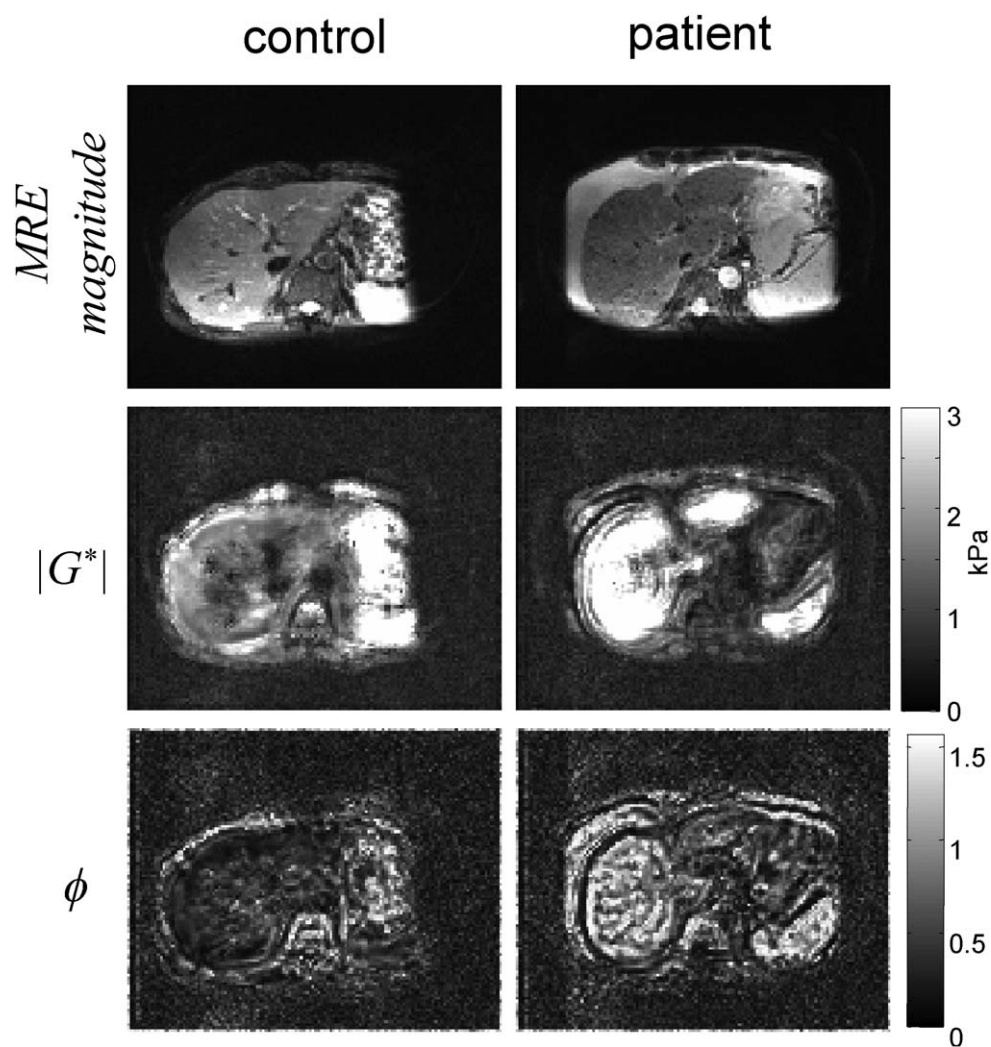


FIG. 7. MRE data of a healthy volunteer and patient #1. Central image slices are shown for the magnitude of the MRE signal,  $|G^*|$ , and  $\phi$ .

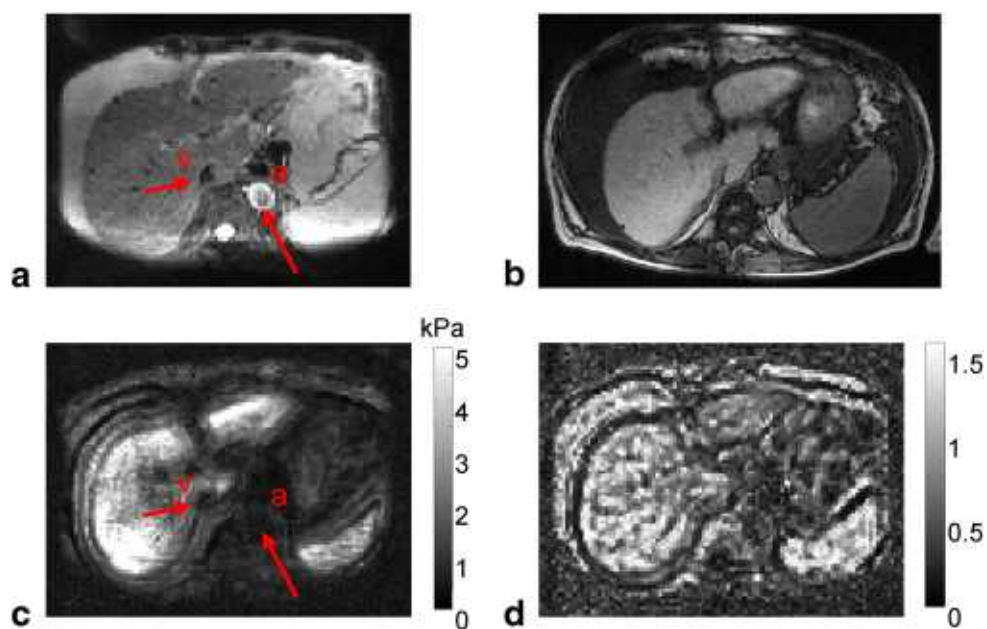


FIG. 8. Central slice from the MRE data set of patient #1 shown in Figure 7, magnitude of the MRE signal (a),  $T_1$ -weighted anatomical image (b),  $|G^*|$  (c), and  $\phi$  (d). Inferior vena cava and descending aorta are pointed by arrows, labeled with “v” and “a,” respectively. Contrast is adjusted in  $|G^*|$  for anatomic details. Note that due to different slice thickness, (b) has a similar but not identical slice position as (a), (c), (d). [Color figure can be viewed in the online issue, which is available at [wileyonlinelibrary.com](http://wileyonlinelibrary.com).]

Table 1  
Spatially Averaged MRE Parameters  $|G^*|$  and  $\phi$  of Liver and Spleen of All Subjects (Standard Deviations [SD] Are Given in Brackets)

No.	Age (years)	Sex	Liver		Spleen	
			G*  in kPa	$\phi$	G*  in kPa	$\phi$
Healthy volunteers						
1a	27	M	1.479 (0.550)	0.435 (0.218)	3.271 (1.144)	0.628 (0.270)
1b			1.547 (0.474)	0.353 (0.184)	3.870 (1.465)	0.490 (0.254)
1c			1.475 (0.466)	0.402 (0.206)	3.631 (1.331)	0.437 (0.215)
1d			1.704 (0.709)	0.476 (0.218)	2.872 (0.874)	0.562 (0.300)
1e			1.689 (0.626)	0.430 (0.198)	2.972 (0.874)	0.562 (0.300)
Mean #1			1.579 (0.565 <sup>a</sup> )	0.419 (0.204 <sup>a</sup> )	3.323 (1.138 <sup>a</sup> )	0.536 (0.269 <sup>a</sup> )
2	40	M	1.303 (0.449)	0.551 (0.276)	1.600 (0.534)	0.886 (0.338)
3	42	M	1.763 (0.663)	0.426 (0.203)	4.034 (1.581)	0.570 (0.217)
4	26	M	1.653 (0.583)	0.468 (0.229)	3.194 (1.024)	0.683 (0.295)
5	28	M	1.321 (0.506)	0.545 (0.276)	1.824 (0.609)	0.745 (0.306)
6	51	M	1.012 (0.387)	0.592 (0.309)	1.154 (0.316)	0.886 (0.352)
7	26	M	1.328 (0.474)	0.517 (0.283)	2.209 (0.530)	0.877 (0.355)
8	22	F	1.569 (0.661)	0.454 (0.237)	1.724 (0.425)	0.952 (0.352)
9	22	F	1.293 (0.570)	0.534 (0.267)	1.195 (0.327)	0.649 (0.298)
10	29	F	1.607 (0.548)	0.412 (0.185)	2.639 (1.016)	0.715 (0.302)
Mean			1.443 (0.227 <sup>b</sup> )	0.492 (0.064 <sup>b</sup> )	2.290 (0.975 <sup>b</sup> )	0.749 (0.145 <sup>b</sup> )
Patients						
1	61	F	3.361 (1.818)	0.880 (0.347)	3.551 (1.397)	1.062 (0.308)
2	58	F	1.882 (1.296)	0.826 (0.357)	2.118 (0.840)	1.126 (0.295)
3	75	M	1.096 (0.532)	0.664 (0.314)	2.526 (0.856)	0.908 (0.327)
4	60	M	1.487 (0.622)	0.842 (0.344)	2.140 (0.706)	0.949 (0.371)
Mean			1.956 (0.990 <sup>b</sup> )	0.803 (0.096 <sup>b</sup> )	2.584 (0.672 <sup>b</sup> )	1.012 (0.101 <sup>b</sup> )

Volunteer #1 was investigated five times for testing the reproducibility of the method.

<sup>a</sup>SD values correspond to the mean of five SD-values of volunteer #1 given in the rows above.

<sup>b</sup>Inter-individual SD of the group-mean of  $|G^*|$  and  $\phi$ .

MRE in clinical radiological examinations and permit precise noninvasive staging of hepatic fibrosis.

## ACKNOWLEDGMENTS

Sebastian Hirsch and Jing Guo contributed equally to this article as first authors.

## REFERENCES

- Parker KJ, Fu D, Graceswki SM, Yeung F, Levinson SF. Vibration sonoelastography and the detectability of lesions. *Ultrasound Med Biol* 1998;24:1437–1447.
- Ophir J, Cespedes I, Ponnekanti H, Yazdi Y, Li X. Elastography: a quantitative method for imaging the elasticity of biological tissues. *Ultrason Imaging* 1991;13:111–134.
- Muthupillai R, Lomas DJ, Rossman PJ, Greenleaf JF, Manduca A, Ehman RL. Magnetic resonance elastography by direct visualization of propagating acoustic strain waves. *Science* 1995;269:1854–1857.
- Plewes DB, Betty I, Urchuk SN, Soutar I. Visualizing tissue compliance with MR imaging. *J Magn Reson Imaging* 1995;5:733–738.
- Friedrich-Rust M, Ong MF, Herrmann E, Dries V, Samaras P, Zeuzem S, Sarrazin C. Real-time elastography for noninvasive assessment of liver fibrosis in chronic viral hepatitis. *AJR Am J Roentgenol* 2007;188:758–764.
- Sandrin L, Fourquet B, Hasquenoph JM, et al. Transient elastography: a new noninvasive method for assessment of hepatic fibrosis. *Ultrasound Med Biol* 2003;29:1705–1713.
- Palmeri ML, Wang MH, Dahl JJ, Frinkley KD, Nightingale KR. Quantifying hepatic shear modulus in vivo using acoustic radiation force. *Ultrasound Med Biol* 2008;34:546–558.
- Rouviere O, Yin M, Dresner MA, Rossman PJ, Burgart LJ, Fidler JL, Ehman RL. MR elastography of the liver: preliminary results. *Radiology* 2006;240:440–448.
- Huwart L, Peeters F, Sinkus R, Annet L, Salameh N, ter Beek LC, Horsmans Y, Van Beers BE. Liver fibrosis: non-invasive assessment with MR elastography. *NMR Biomed* 2006;19:173–179.
- Klatt D, Asbach P, Rump J, Papazoglou S, Somasundaram R, Modrow J, Braun J, Sack I. In vivo determination of hepatic stiffness using steady-state free precession magnetic resonance elastography. *Invest Radiol* 2006;41:841–848.
- Bonekamp S, Kamel I, Solga S, Clark J. Can imaging modalities diagnose and stage hepatic fibrosis and cirrhosis accurately? *J Hepatol* 2009;50:17–35.
- Nedredal GI, Yin M, McKenzie T, Lillegard J, Luebke-Wheeler J, Talwalkar J, Ehman R, Nyberg SL. Portal hypertension correlates with splenic stiffness as measured with MR elastography. *J Magn Reson Imaging* 2011;34:79–87.
- Huwart L, Sempoux C, Vicaute E, et al. Magnetic resonance elastography for the noninvasive staging of liver fibrosis. *Gastroenterology* 2008;135:32–40.
- Yin M, Talwalkar JA, Glaser KJ, Manduca A, Grimm RC, Rossman PJ, Fidler JL, Ehman RL. Assessment of hepatic fibrosis with magnetic resonance elastography. *Clin Gastroenterol Hepatol* 2007;5:1207–1213 e1202.
- Asbach P, Klatt D, Hamhaber U, Braun J, Somasundaram R, Hamm B, Sack I. Assessment of liver viscoelasticity using multifrequency MR elastography. *Magn Reson Med* 2008;60:373–379.
- Uffmann K, Abicht C, Grote W, Quick HH, Ladd ME. Design of an MR-Compatible piezoelectric actuator for MR elastography. *Concept Magnetic Res* 2002;15:239–254.
- Chopra R, Arani A, Huang Y, Musquera M, Wachsmuth J, Bronskill M, Plewes D. In vivo MR elastography of the prostate gland using a transurethral actuator. *Magn Reson Med* 2009;62:665–671.
- Manduca A, Oliphant TE, Dresner MA, Mahowald JL, Kruse SA, Amromin E, Felmlee JP, Greenleaf JF, Ehman RL. Magnetic resonance elastography: non-invasive mapping of tissue elasticity. *Med Image Anal* 2001;5:237–254.
- Manduca A, Lake DS, Kruse SA, Ehman RL. Spatio-temporal directional filtering for improved inversion of MR elastography images. *Med Image Anal* 2003;7:465–473.
- Oliphant TE, Manduca A, Ehman RL, Greenleaf JF. Complex-valued stiffness reconstruction for magnetic resonance elastography by algebraic inversion of the differential equation. *Magn Reson Med* 2001;45:299–310.
- Van Houten EE, Paulsen KD, Miga MI, Kennedy FE, Weaver JB. An overlapping subzone technique for MR-based elastic property reconstruction. *Magn Reson Med* 1999;42:779–786.

22. Van Houten EEW, Viviers Dv, McGarry MD, Perrinez PR, Perreard II, Weaver JB, Paulsen KD. Subzone based magnetic resonance elastography using a Rayleigh damped material model. *Med Phys* 2011;38:1993.
23. Baghani A, Salcudean S, Honarvar M, Sahebjavaher RS, Rohling R, Sinkus R. Travelling wave expansion: a model fitting approach to the inverse problem of elasticity reconstruction. *IEEE Trans Med Imaging* 2011;30:1555–1565.
24. Okamoto RJ, Clayton EH, Bayly PV. Viscoelastic properties of soft gels: comparison of magnetic resonance elastography and dynamic shear testing in the shear wave regime. *Phys Med Biol* 2011;56:6379–6400.
25. Papazoglou S, Hirsch S, Braun J, Sack I. Multifrequency inversion in magnetic resonance elastography. *Phys Med Biol* 2012;57:2329–2346.
26. Klatt D, Friedrich C, Korth Y, Vogt R, Braun J, Sack I. Viscoelastic properties of liver measured by oscillatory rheometry and multifrequency magnetic resonance elastography. *Biorheology* 2010;47:133–141.
27. Posnansky O, Guo J, Hirsch S, Papazoglou S, Braun J, Sack I. Fractal network dimension and viscoelastic powerlaw behavior: I. A modeling approach based on a coarse-graining procedure combined with shear oscillatory rheometry. *Phys Med Biol* 2012;57:4023–4040.
28. Gurtovenko AA, Blumen A. Generalized Gaussian structures: models for polymer systems with complex topologies. *Polymer analysis, polymer theory*, Vol. 182. *Advances in Polymer Science*. Berlin: Springer; 2005. p 171–282.
29. Kruse SA, Smith JA, Lawrence AJ, Dresner MA, Manduca A, Greenleaf JF, Ehman RL. Tissue characterization using magnetic resonance elastography: preliminary results. *Phys Med Biol* 2000;45:1579–1590.
30. Klatt D, Hamhaber U, Asbach P, Braun J, Sack I. Noninvasive assessment of the rheological behavior of human internal organs using multifrequency MR elastography: a study of brain and liver viscoelasticity. *Phys Med Biol* 2007;52:7281–7294.
31. Asbach P, Klatt D, Schlosser B, et al. Viscoelasticity-based staging of hepatic fibrosis with multifrequency MR elastography. *Radiology* 2010;257:80–86.
32. Rump J, Klatt D, Braun J, Warmuth C, Sack I. Fractional encoding of harmonic motions in MR elastography. *Magn Reson Med* 2007;57:388–395.
33. Papazoglou S, Xu C, Hamhaber U, Siebert E, Bohner G, Klingebiel R, Braun J, Sack I. Scatter-based magnetic resonance elastography. *Phys Med Biol* 2009;54:2229–2241.
34. Hirsch S, Posnansky O, Papazoglou S, Elgeti T, Braun J, Sack I. Measurement of vibration-induced volumetric strain in the human lung. *Magn Reson Med* 2013;69:667–674.
35. Anderssen RS, Hegland M. For numerical differentiation, dimensionality can be a blessing! *Math Comput* 1999;68:1121–1141.
36. McLaughlin JR, Zhang N, Manduca A. Calculating tissue shear modulus and pressure by 2D Log-Elastographic methods. *Inverse Problems* 2010;26.
37. Sinkus R, Tanter M, Catheline S, Lorenzen J, Kuhl C, Sondermann E, Fink M. Imaging anisotropic and viscous properties of breast tissue by magnetic resonance-elastography. *Magn Reson Med* 2005;53:372–387.
38. Lemke AJ, Brinkmann MJ, Schott T, Niehues SM, Settmacher U, Neuhäus P, Felix R. Living donor right liver lobes: preoperative CT volumetric measurement for calculation of intraoperative weight and volume. *Radiology* 2006;240:736–742.
39. Clayton EH, Garbow JR, Bayly PV. Frequency-dependent viscoelastic parameters of mouse brain tissue estimated by MR elastography. *Phys Med Biol* 2011;56:2391–2406.
40. Huwart L, Sempoux C, Salameh N, et al. Liver fibrosis: noninvasive assessment with MR elastography versus aspartate aminotransferase-to-platelet ratio index. *Radiology* 2007;245:458–466.
41. Talwalkar JA, Yin M, Venkatesh S, Rossman PJ, Grimm RC, Manduca A, Romano A, Kamath PS, Ehman RL. Feasibility of in vivo MR elastographic splenic stiffness measurements in the assessment of portal hypertension. *AJR Am J Roentgenol* 2009;193:122–127.
42. Huwart L, Salameh N, ter Beek L, Vicaut E, Peeters F, Sinkus R, Van Beers BE. MR elastography of liver fibrosis: preliminary results comparing spin-echo and echo-planar imaging. *Eur Radiol* 2008;18:2535–2541.
43. Yin M, Rouviere O, Glaser KJ, Ehman RL. Diffraction-biased shear wave fields generated with longitudinal magnetic resonance elastography drivers. *Magn Reson Imaging* 2008;26:770–780.
44. Yin M, Talwalkar JA, Glaser KJ, Venkatesh SK, Chen J, Manduca A, Ehman RL. Dynamic postprandial hepatic stiffness augmentation assessed with MR elastography in patients with chronic liver disease. *AJR Am J Roentgenol* 2011;197:64–70.